The Astrophysical Journal Letters, 892:L13 (5pp), 2020 March 20 https://doi.org/10.3847/2041-8213/ab7d3f

The Critical Role of Collisionless Plasma Energization on the Structure of Relativistic Magnetic Reconnection

Yi-Hsin Liu[1], Shan-Chang Lin[1], Michael Hesse[2,3], Fan Guo[4], Xiaocan Li[1,4], Haocheng Zhang[5], and Sarah Peery[1]
[1] Dartmouth College, Hanover, NH 03750, USA; Yi-Hsin.Liu@dartmouth.edu
[2] University of Bergen, Bergen, Norway
[3] Southwest Research Institute, San Antonio, TX 78238, USA
[4] Los Alamos National Laboratory, Los Alamos, NM 87545, USA
[5] Purdue University, West Lafayette, IN 47907, USA
Received 2020 February 11; revised 2020 March 6; accepted 2020 March 6; published 2020 March 25

Abstract

During magnetically dominated relativistic reconnection, inflowing plasma depletes the initial relativistic pressure at the x-line and collisionless plasma heating inside the diffusion region is insufficient to overcome this pressure loss. The resulting significant pressure drop causes a collapse at the x-line, essentially a localization mechanism of the diffusion region necessary for fast reconnection. The extension of this low-pressure region (into the outflow) further explains the bursty nature of antiparallel reconnection because a once opened outflow exhaust can also collapse, which repeatedly triggers secondary tearing islands. However, a stable single x-line reconnection can be achieved when an external guide field exists, since the reconnecting magnetic field component rotates out of the reconnection plane at outflows, providing additional magnetic pressure to keep the exhaust open.

Unified Astronomy Thesaurus concepts: Plasma astrophysics (1261); Plasma physics (2089)

1. Introduction

The past decade has seen a dramatic surge of interest in the potential role of magnetically dominated reconnection (where the magnetic energy density to the enthalpy density ratio $\sigma \equiv B_0^2/(4\pi w) \gg 1$) in powering strong particle acceleration and high-energy radiation in various astrophysical environments (Guo et al. 2014, 2019; Sironi & Spitkovsky 2014; Werner et al. 2016), including super-flares in pulsar winds (Abdo et al. 2011; Tavani et al. 2011; Uzdensky et al. 2011; Arons 2012), accretion disks and jets emanating from rotating compact objects, and their merging events (Giannios et al. 2009; Zhang & Yan 2011; McKinney & Uzdensky 2012; Guo et al. 2016; Zhang et al. 2018). Magnetic reconnection breaks and rejoins magnetic field lines inside the *diffusion region* that dwells in current sheets. By virtue of the *frozen-in* condition between plasmas and magnetic flux outside the diffusion region, a continuous reconnection process inherently involves the transient motion of particles passing through this diffusion region from the inflow to the outflow areas. Notably, inside a planar high-σ current sheet, the pressure needs to be relativistic to balance the strong upstream magnetic pressure; i.e., $P_{\rm sheet} \approx B_0^2/8\pi$. This balanced pressure during reconnection is often assumed in theoretical models (e.g., Blackman & Field 1994; Lyubarsky 2005; Parker 1957; Uzdensky et al. 2010). However, it is questionable whether the reconnection diffusion region can provide sufficient thermal heating to sustain this relativistic pressure under a constant inflow of low-pressure (i.e., compared to $B_0^2/8\pi$) plasmas. Understanding this force-balance is critical in determining the structure of the reconnection layer, which ultimately decides particle acceleration during reconnection and its radiation signatures.

In this Letter, we demonstrate that a significant pressure drop occurs at the magnetic x-line, $P_{x\rm line} \ll B_0^2/8\pi$, in kinetic simulations of high-σ magnetic reconnection. We then perform analyses to show that collisionless plasma heating inside the diffusion region is insufficient to sustain a thermal pressure to balance the strong magnetic pressure far upstream. This plays a key role in determining the geometry of the reconnection layer as it provides a *localization mechanism* that limits the length of the diffusion region, and is essential for facilitating fast magnetic reconnection (Biskamp & Schwarz 2001).[6] On the other hand, numerical simulations also reveal that relativistic reconnection in the antiparallel geometry is characterized by repetitive bursts of magnetic islands (Guo et al. 2015; Sironi et al. 2016), but a more stable single x-line is possible with an external guide field (Ball et al. 2019; Rowan et al. 2019). We point out that this morphology difference can be explained by the change of the outflow magnetic structure and the pressure balance across exhausts.

2. Simulation Setup

The initial magnetic field $\boldsymbol{B} = B_{x0}[\tanh(z/\lambda)\hat{\boldsymbol{x}} + b_g\hat{\boldsymbol{y}}]$. Electron–positron plasmas are believed to be relevant in highly energetic astrophysical systems such as extragalactic jets (Wardle et al. 1998) and pulsar winds (Sturrock 1971; Arons 2012), thus we use electron–positron pairs that have mass $m_i = m_e \equiv m$. Each species has a distribution $f_h \propto \mathrm{sech}^2(z/\lambda)\exp[-\gamma_d(\gamma_L mc^2 \pm mV_d u_y)/T']$ in the simulation frame, which is a component with a peak density n_0' and temperature T' boosted by a drift velocity $\pm V_d$ in the y-direction for ions and electrons, respectively. In this Letter, the primed quantities are measured in the fluid rest (proper) frame, while the unprimed quantities are measured in the simulation frame unless otherwise specified. Here $\boldsymbol{u} = \gamma_L \boldsymbol{v}$ is the 4-velocity, $\gamma_L = 1/[1-(v/c)^2]^{1/2}$ is the Lorentz factor of a particle, and $\gamma_d \equiv 1/[1-(V_d/c)^2]^{1/2}$. The drift velocity is determined by Ampére's law $cB_{x0}/(4\pi\lambda) = 2e\gamma_d n_0' V_d$. The temperature is determined by the pressure balance $B_{x0}^2/(8\pi) = 2n_0'T'$. The resulting density in the simulation frame is $n_0 = \gamma_d n k_0'$. In addition, a non-drifting background

[6] Note that even if a similar fast rate $\sim\mathcal{O}(0.1)$ is observed, the localization mechanism can be different in different systems (Liu et al. 2018).

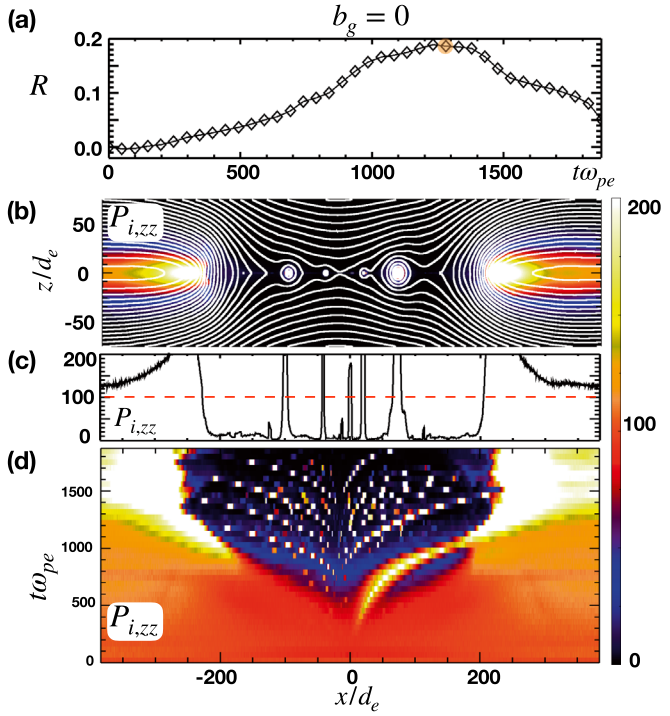

Figure 1. $b_g = 0$ case. (a) Evolution of the reconnection rate R. (b) The pressure component $P_{i,zz}$ overlaid with A_y contours at time $1250/\omega_{pe}$ and (c) its cut along $z = 0$ where the red dashed line marks the initial value. (d) The time-stack plot of $z = 0$ cuts. Pressures are normalized to $n_b mc^2$, and the color map is capped by the value 200.

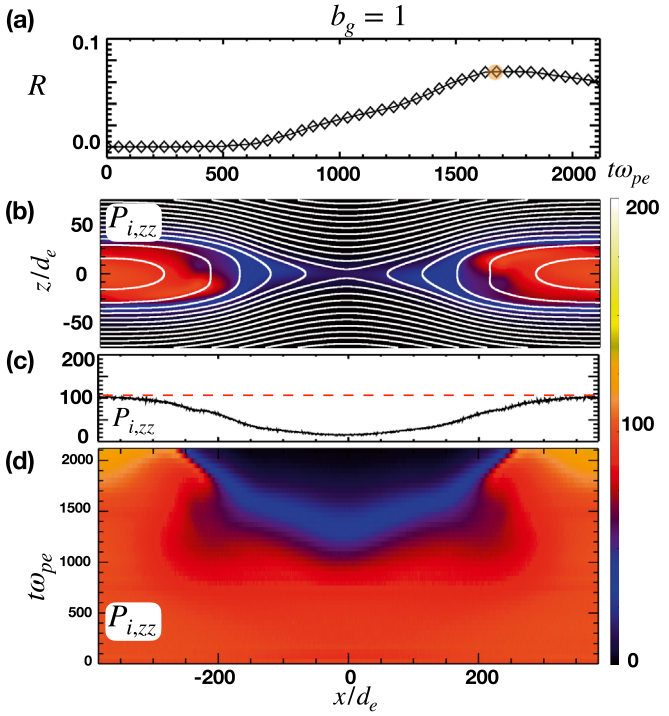

Figure 2. $b_g = 1$ case. (a) Evolution of the reconnection rate R. (b) The pressure component $P_{i,zz}$ overlaid with A_y contours at time $1650/\omega_{pe}$ and (c) its cut along $z = 0$ in where the red dashed line marks the initial value. (d) The time-stack plot of $z = 0$ cuts.

component $f_b \propto \exp(-\gamma_L mc^2/T_b)$ with a uniform density n_b is included. The simulations are performed using Vector Particle-in-Cell (VPIC; Bowers et al. 2009), which solves the fully relativistic dynamics of particles and electromagnetic fields. Densities, times, velocities, lengths, and pressures are normalized by the background density n_b, the plasma frequency $\omega_{pe} \equiv (4\pi n_b e^2/m_e)^{1/2}$, the light speed c, the inertia length $d_e \equiv c/\omega_{pe}$, and $n_b mc^2$, respectively. The boundary conditions are periodic in the x-direction, while in the z-direction the field boundary condition is conducting and the particles are reflected at the boundaries. The domain size is $L_x \times L_z = 768d_e \times 768d_e$ with $6144 \times 12{,}288$ cells. There are 100 particles per cell. To better illustrate the pressure collapse, we use a rather thick initial sheet with a half-thickness $\lambda = 20d_e$. The background $n_b = n_0'$, $T_b/m_e c^2 = 0.5$, and $\omega_{pe}/\Omega_{ce} = 0.05$ where $\Omega_{ce} \equiv eB_{x0}/(m_e c)$ is a cyclotron frequency. The magnetization parameter $\sigma \equiv B_0^2/(4\pi w)$ is defined using the upstream (background) quantities $w = 2n_b mc^2 + 2(\Gamma/(\Gamma - 1))n_b T_b$ with the ratio of specific heats $\Gamma = 5/3$. The reconnecting component contributes to $\sigma_x \equiv B_{x0}^2/(4\pi w) = (\Omega_{ce}/\omega_{pe})^2/\{2[1 + (\Gamma/(\Gamma - 1))(T_b/mc^2)]\} = 88.9$. In this work, we compare the antiparallel case ($b_g = 0$) and a guide field case with $b_g = 1$.

3. Results

3.1. The Pressure Depletion at the x-line

The antiparallel case is discussed in Figure 1. Panel (a) shows the evolution of the normalized reconnection rate $R \equiv \partial_t \Psi/B_{x0} V_{Ax0}$, where $\Psi = \max(A_y) - \min(A_y)$ along $z = 0$ and A_y is the y-component of the vector potential. The Alfvén speed in the x-direction is $V_{Ax0} = c[\sigma_x/(1 + \sigma_x + \sigma_g)]^{1/2}$ (Liu et al. 2015). The reconnection rate reaches the typical fast rate of order 0.1 (Cassak et al. 2017; Liu et al. 2017). The pressure component $P_{i,zz}$ responsible for the pressure balance across the current sheet is shown in (b), its cut along $z = 0$ in (c), and the time-stack plot of $z = 0$ cuts in (d). Here we employ Wright and Hadley's (Wright & Hadley 1975; Hesse & Zenitani 2007; Zenitani 2018) definition of pressure tensor $\overleftrightarrow{P} \equiv \int d^3u \boldsymbol{vu} f - n\boldsymbol{VU}$ where $\boldsymbol{V} \equiv (1/n)\int d^3u \boldsymbol{v} f$ and $\boldsymbol{U} \equiv (1/n)\int d^3u \boldsymbol{u} f$. The pronounced feature is a significant drop of pressure (dark area, up to $\times\mathcal{O}(100)$ smaller) at both the x-line and outflow exhausts when the system evolves toward its nonlinear stage, and it is accompanied with the bursty generation of secondary tearing islands. This pressure drop occurs as the inflowing low-pressure plasma from upstream depletes the pressure around the diffusion region. For the $b_g = 1$ case (Figure 2), the pressure drop is also evident. An important difference to the antiparallel case is the stable single x-line with a similar fast rate but without multiple magnetic islands. While not being the focus of this work, interestingly, the thickness of the diffusion region becomes much broader in the $b_g = 1$ case likely due to the current starvation effect and incompressibility associated with a guide field (Zenitani & Hesse 2008). Note that this pressure depletion and the conclusions hereafter not only apply to Harris-type current sheets, but also to (initially) force-free current sheets (Guo et al. 2014, 2015; Liu et al. 2015), because the initial magnetic pressure therein will also be expelled out to the downstream in the nonlinear stage.

3.2. Pressure Depletion as a Localization Mechanism

In Figure 3, we illustrate the need of localization when the thermal pressure drops right at the x-line. During reconnection, the total pressure at the x-line is depleted by the inflowing low-pressure plasmas. The red areas in panels (a) and (b) indicate

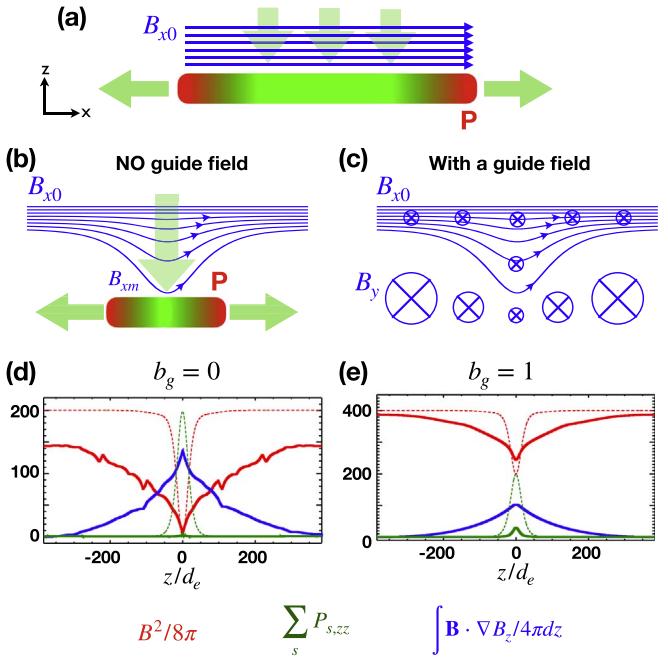

Figure 3. Pressure depletion vs. x-line localization. Green arrows indicate the flow pattern inherent to reconnection. The initial high pressure plasmas are in red, the depleted plasma pressure in green. (a) An elongated diffusion region. (b) A localized diffusion region. (c) The effect of the guide field. (d) The analysis of the force-balance (Equation (1)) across the primary x-line of the antiparallel case, and (e) for the $b_g = 1$ case. Dashed curves show the initial profiles for comparison.

the original pressure that is high enough to balance the magnetic pressure upstream of the planar current sheet. The green areas indicate low-pressure plasmas that flow in from upstream regions. If the pressure depletion cannot be overcome by the thermal heating inside the diffusion region, then an elongated diffusion region in panel (a), is not an option for a steady-state solution because the green region will collapse. The only way to restore the force-balance along the inflow is to develop a localized geometry as shown in panel (b), because the indented upstream magnetic field implies a tension force pointing to the upstream, acting against the magnetic pressure $B_{x0}^2/8\pi$. Note that the geometry in panels (b) and (c) with an opened outflow exhaust implies a diffusion region of limited length, i.e., a *localized* diffusion region. A more localized diffusion region induces a faster inflow and thus a stronger pressure depletion[7] to localize the diffusion region; these steps form a dynamical loop of positive feedback. One may consider that some other mechanisms, such as secondary tearing modes, localize the diffusion region and deplete the pressure therein accordingly, but it is difficult to explain why the pressure inside the entire exhaust is depleted as well, as seen between $x/d_e \in [-200, 200]$ in Figures 1(b) and (c).

To demonstrate the correlation between the pressure drop and localization, we analyze the force-balance that can be derived from the momentum equation (Hesse & Zenitani 2007) $mn_s\partial_t \boldsymbol{U}_s + mn_s\boldsymbol{V}_s\cdot\nabla\boldsymbol{U}_s = -\nabla\cdot\overleftrightarrow{P}_s + q_s n_s\boldsymbol{E} + q_s n_s(\boldsymbol{V}_s\times\boldsymbol{B}/c)$. By summing up the momentum equations of the two species ($s = e, i$), we obtain $\nabla B^2/8\pi + \sum_s \nabla\cdot\overleftrightarrow{P}_s - \boldsymbol{B}\cdot\nabla\boldsymbol{B}/4\pi + \sum_s mn_s\boldsymbol{V}_s\cdot\nabla\boldsymbol{U}_s + \sum_s mn_s\partial_t\boldsymbol{U}_s - \sum_s q_s n_s\boldsymbol{E} + \partial_t\boldsymbol{E}/(4\pi c) = 0$. Across the x-line along the inflow (z-) direction, the dominant terms are integrated to give

$$\frac{B^2}{8\pi} + \sum_s P_{s,zz} - \int_{-L_z/2}^{z}\frac{\boldsymbol{B}\cdot\nabla B_z}{4\pi}dz' \simeq \text{const.} \quad (1)$$

As shown in Figure 3(d), the initial (dashed curves) hot $\sum_s P_{s,zz}$ (green) can balance the upstream $B^2/8\pi$ (red). Later (solid curves), $\sum_s P_{s,zz}$ drops significantly and the only term that can balance $B^2/8\pi$ is the tension force (blue) pointing to the upstream. This captures the effect of the indenting upstream magnetic field illustrated in panel (b), essentially the localization of the diffusion region (Liu et al. 2017). A similar balance is observed with a guide field in panel (e), but an important difference at outflow exhausts will be discussed later.

3.3. The Thermal Heating Efficiency toward the x-line

If P_{zz} at the x-line is smaller than $B_{x0}^2/8\pi$, it leads to a localized geometry, regardless of the initial thickness (2δ) or the profile of the current sheet. The question is then why the x-line heating is insufficient to overcome this pressure loss. Per Poynting's theorem, $\boldsymbol{J}\cdot\boldsymbol{E}$ measures the energy conversion rate from electromagnetic energy to plasma energies. Dotting the momentum equations with $\boldsymbol{V}_s$ then summing up the species, we get $\boldsymbol{J}\cdot\boldsymbol{E} = \sum_s mn_s\boldsymbol{V}_s\cdot(\boldsymbol{V}_s\cdot\nabla)\boldsymbol{U}_s + \sum_s \boldsymbol{V}_s\cdot(\nabla\cdot\overleftrightarrow{P}_s) + \sum_s mn_s\boldsymbol{V}_s\cdot\partial_t\boldsymbol{U}_s$. Integrating the energy gain of plasmas along its path (at $x = 0$) toward the x-line, we find the dominant terms in the nonlinear state:

$$\int(\boldsymbol{J}\cdot\boldsymbol{E})dt = \int_{-L_z/2}^{z}(\boldsymbol{J}\cdot\boldsymbol{E})\frac{dz'}{V_z} \simeq \sum_s mn_s\frac{V_{s,y}U_{s,y}}{2} + \sum_s P_{s,zz} + \int\sum_s V_{s,y}(\nabla\cdot\overleftrightarrow{P}_s)_y\frac{dz'}{V_z}. \quad (2)$$

This integral has a singularity near the vicinity of the x-line where $V_z \to 0$, which exactly arises from the last term of the right-hand side of Equation (2), i.e., because $E_y = (1/q_s n_s)(\nabla\cdot\overleftrightarrow{P}_s)_y$ (Bessho & Bhattacharjee 2005; Kagan et al. 2013; Hesse et al. 2011) right at the x-line, so that $\boldsymbol{J}\cdot\boldsymbol{E} \simeq \sum_s V_{s,y}(\nabla\cdot\overleftrightarrow{P}_s)_y$. We remove the contribution from this term[8] in the integral and plot it as orange curves in Figure 4 for both the $b_g = 0$ and $b_g = 1$ cases. These orange curves follow reasonably well with the profiles of $\sum_s mn_s V_{s,y}U_{s,y}/2 + \sum_s P_{s,zz}$ in light blue. By comparing the light blue and green curves, we realize that the magnetic energy is mostly converted to the bulk flow kinetic energy in the current (y-) direction, while only a small portion to the thermal pressure in the z-direction, $\sum_s P_{s,zz}$.

On the other hand, the available energy seen by the inflowing plasma can be estimated as $\int(\boldsymbol{J}\cdot\boldsymbol{E})dt \sim J_y E_y\Delta t \sim (c/4\pi)(B_{x0}/\delta)(V_{\rm in}B_{x0}/c)\ (\delta/V_{\rm in}) \sim \mathcal{O}(B_{x0}^2/4\pi)$. Here $\Delta t \sim \delta/V_{\rm in}$ is the average timescale spent by a particle in the diffusion region (Hesse et al. 2011). The peak value of plasma energy gain (light blue) is indeed limited by $\mathcal{O}(B_{x0}^2/4\pi) = 400$ as shown in Figure 4. From these observations, we conclude that if most energy is converted to the bulk kinetic energy of the current

[7] Note that the electric field strength is upper bounded by the fast rate $\simeq 0.1B_{x0}V_A$ (Liu et al. 2017).

[8] Note that a larger $(\nabla\cdot\overleftrightarrow{P}_s)_y$ does not help with the pressure balance in the z-direction even in the nonrelativistic limit where $\overleftrightarrow{P}_s$ is symmetric, because $\partial_y P_{s,yz} = 0$ in 2D.

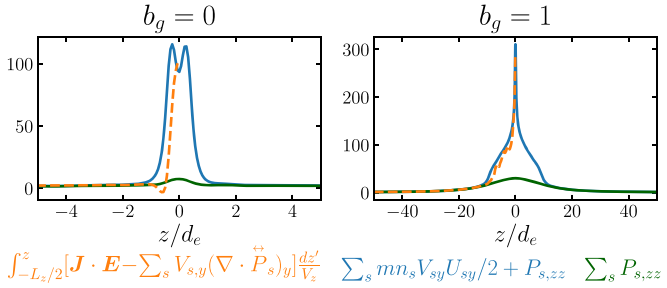

Figure 4. The heating efficiency (Equation (2)) analysis across the primary x-line. The $b_g = 0$ case ($b_g = 1$ case) is on the left (right).

carrier, then right at the x-line $\sum_s P_{s,zz} < B_{x0}^2/8\pi$; the diffusion region needs to be localized. It is interesting to remark that this kinetic description is different from that of resistive-MHD models. In MHD, inflowing plasma does not need to be turned into current carriers and thus no energy is required to sustain the current. Consequently, such localization mechanisms may be absent in resistive-MHD.

3.4. *Bursty Multiple* x*-lines versus Stable Single* x*-line*

The preferential pressure depletion right at the x-line localizes the diffusion region. For this geometry to be *stable*, it *also* requires a balanced pressure across the exhaust; i.e., it needs the original high pressure (red) at outflows (Figure 3(b)). Although the plasma will be further heated while being accelerated into outflow exhausts, the exhaust-heating in this antiparallel case (Figure 1), however, also appears unable to bring the pressure back to the original value. A once opened exhaust will thus collapse, triggering copious fast-growing secondary magnetic islands, forming competing multiple x-lines. In other words, the reconnection layer in this regime is squeezed to make islands, likely not caused by the commonly referenced plasmoid instability (Loureiro et al. 2007), that is calculated based on an equilibrium current sheet. The growth of magnetic islands helps establish the localization (Figure 3(b)) locally for each individual x-line, but those islands can be expelled out by the primary outflows from the dominant x-line (near the center of simulation domain). Thus, the generation of magnetic islands inside the reconnection layer is bursty and repetitive, as clearly seen in Figure 1(d). One may argue that these tearing modes cause the localization, but they are in fact secondary effects immersed inside the large-scale localization (i.e., concentric darker area in Figure 5(b)) due to the pressure depletion. This aspect becomes clearer in guide field reconnection where secondary tearing modes can be avoided but the system still achieves a localized geometry. Due to the symmetry, an out-of-plane magnetic field is not generated in the antiparallel case in Figure 5(a). However, with a guide field the reconnecting field, once reconnects, can simply rotate to the out-of-plane direction and provide the (magnetic) pressure needed for supporting opened outflow exhausts. This is seen in Figures 5(c) and (d) along outflows, and the idea is illustrated in Figure 3(c) where a larger $\otimes$ symbol indicates a stronger out-of-plane field. These structures are consistent with Petschek's solution at outflows; in the antiparallel case, the outflow exhaust is bounded by a pair of co-planar (i.e., no B_y at downstream) slow shocks (Petschek 1964; Lin & Lee 1993; Lyubarsky 2005), which turns into a pair of rotational discontinuities (that preserve the magnetic pressure) in the guide field case (e.g., Levy et al. 1964; Lin & Lee 1993; Lyubarsky 2005; Liu et al. 2011). This additional source of magnetic pressure (Figure 5(c)) inside the exhaust makes a stable single x-line reconnection possible, in sharp contrast to the bursty antiparallel case.

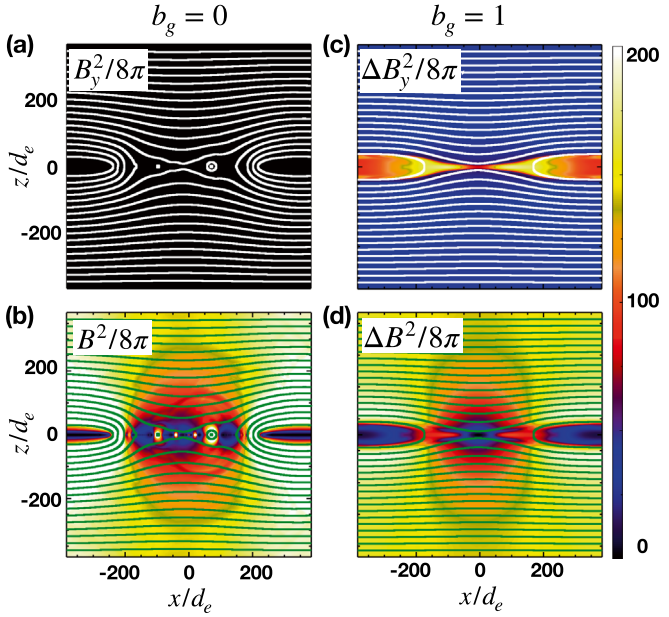

Figure 5. The $b_g = 0$ cases ($b_g = 1$ cases) in the left (right) column. Top and bottom rows show the out-of-plane magnetic pressure $B_y^2/8\pi$ and the total magnetic pressure $B^2/8\pi$ overlaid with A_y contours, respectively. In panels (c) and (d), the magnetic pressure difference from their minimum values are shown for the $b_g = 1$ case. The color map in panel (b) is capped by the value 200. The concentric $B^2/8\pi$ dip around the x-line best illustrates the localization.

4. Summary and Discussion

In strongly magnetized plasmas, there is an intriguing linkage between the heating efficiency inside the reconnection diffusion region and its localization mechanism, which is needed for fast reconnection. We analyze the force-balance across the x-line of relativistic reconnection with and without a guide field. For both cases, significant pressure drops from the original equilibrium value are observed at the x-line. The inflowing plasma gains mostly the bulk kinetic energy in the out-of-plane direction, while only a small fraction of magnetic energy is converted to build up the pressure in the inflow direction; this may reflect the difficulty of thermal heating (compared to the bulk acceleration) in collisionless plasmas. Meanwhile, the energy available to the plasma flowing into the x-line is limited due to its transient timescale within the diffusion region. Thus we conclude that the thermal heating inside the diffusion region is insufficient to overcome the pressure depletion by the continuous inflowing low-pressure plasma. This pressure drop right at the x-line localizes the diffusion region. Contrary to the common perception on the role of x-line heating, we argue reversely that an insufficient thermal heating at reconnection x-line is a key to fast reconnection. Given some degree of localization, the system easily reaches a state with a reconnection rate close to value $\sim\mathcal{O}(0.1)$ (Liu et al. 2017).

Radiative cooling can further reduce the thermal pressure at the x-line, enhancing the localization. It may also trigger more secondary tearing islands during antiparallel reconnection because the low-pressure region can extend into the outflow.

In nature it is more common to have a finite guide field, and the extra magnetic pressure provided by the field rotation helps support the opening of reconnection exhausts, enabling a stable single x-line. Interestingly, in electron-proton plasmas the Hall quadrupole field also arises from the rotation of the reconnecting magnetic field (Mandt et al. 1994; Drake et al. 2008), and it may play a similar role in providing an additional pressure to support the opened outflow exhaust.[9] This aspect deserves a thorough study both in the high-σ and in the nonrelativistic low-β regimes (that is relevant to NASA's Magnetospheric Multiscale mission (MMS) and Parker Solar Probe).

Y.-H.L. is grateful for support from grants NSF-DoE 1902867 and NASA MMS 80NSSC18K0289. F.G. acknowledges support from DOE through the LDRD program at LANL and DoE/OFES support to LANL, and NASA ATP program through grant NNH17AE68I. X.L.'s contribution is in part supported by NASA under grant NNH16AC60I. Simulations were performed at the National Center for Computational Sciences at ORNL and with LANL institutional computing.

ORCID iDs

Yi-Hsin Liu https://orcid.org/0000-0001-5880-2645
Fan Guo https://orcid.org/0000-0003-4315-3755
Haocheng Zhang https://orcid.org/0000-0001-9826-1759

References

Abdo, A. A., Ackermann, M., Ajello, M., et al. 2011, Sci, 331, 739
Arons, J. 2012, SSRv, 173, 341
Ball, D., Sironi, L., & Ozel, F. 2019, ApJ, 884, 57
Bessho, N., & Bhattacharjee, A. 2005, PhRvL, 95, 245001
Biskamp, D., & Schwarz, E. 2001, PhPl, 8, 4729
Blackman, E. G., & Field, G. B. 1994, PhRvL, 72, 494
Bowers, K., Albright, B., Yin, L., et al. 2009, JPhCS, 180, 012055
Cassak, P. A., Liu, Yi-Hsin, & Shay, M. A. 2017, JPlPh, 83, 715830501
Drake, J. F., Shay, M. A., & Swisdak, M. 2008, PhPl, 15, 042306
Giannios, D., Uzdensky, D. A., & Begelman, M. C. 2009, MNRAS, 395, L29
Guo, F., Li, H., Daughton, W., & Liu, Yi-Hsin 2014, PhRvL, 113, 155005
Guo, F., Li, X., Daughton, W., et al. 2019, ApJL, 879, L23
Guo, F., Li, X., Li, H., et al. 2016, ApJL, 818, L9
Guo, F., Liu, Y.-H., Daughton, W., & Li, H. 2015, ApJ, 806, 167
Hesse, M., Neukirch, T., Schindler, K., Kuznetsova, M., & Zenitani, S. 2011, SSRv, 160, 3
Hesse, M., & Zenitani, S. 2007, PhPl, 14, 112102
Kagan, D., Milosavljevic, M., & Spitkovsky, A. 2013, ApJ, 774, 41
Levy, R. H., Petschek, H. E., & Siscoe, G. L. 1964, AIAAJ, 2, 2065
Lin, Y., & Lee, L. C. 1993, SSRv, 65, 59
Liu, Y.-H., Drake, J. F., & Swisdak, M. 2011, PhPl, 18, 092102
Liu, Y.-H., Guo, F., Daughton, W., Li, H., & Hesse, M. 2015, PhRvL, 114, 095002
Liu, Y.-H., Hesse, M., Guo, F., et al. 2017, PhRvL, 118, 085101
Liu, Y.-H., Hesse, M., Guo, F., Li, H., & Nakamura, T. K. M. 2018, PhPl, 25, 080701
Loureiro, N. F., Schekochihin, A. A., & Cowley, S. C. 2007, PhPl, 14, 100703
Lyubarsky, Y. E. 2005, MNRAS, 358, 113
Mandt, M. E., Denton, R. E., & Drake, J. F. 1994, GeoRL, 21, 73
McKinney, J. C., & Uzdensky, D. A. 2012, MNRAS, 419, 573
Parker, E. N. 1957, JGR, 62, 509
Petschek, H. E. 1964, in Proc. AAS-NASA Symp. NASA-SP 50, The Physics of Solar Flares, ed. W. N. Ness (Washington, DC: NASA), 425
Rowan, M. E., Sironi, L., & Narayan, R. 2019, ApJ, 873, 2
Sironi, L., Giannios, D., & Petropoulou, M. 2016, MNRAS, 462, 48
Sironi, L., & Spitkovsky, A. 2014, ApJL, 783, L21
Sturrock, P. A. 1971, ApJ, 164, 529
Tavani, M., Bulgarelli, A., Vittorini, V., et al. 2011, Sci, 331, 736
Uzdensky, D. A., Cerutti, B., & Begelman, M. C. 2011, ApJL, 737, L40
Uzdensky, D. A., Loureiro, N. F., & Schekochinhin, A. A. 2010, PhRvL, 105, 235002
Wardle, J., Homan, D., Ojha, R., & Roberts, D. H. 1998, Natur, 395, 457
Werner, G. R., Uzdensky, D. A., Cerutti, B., Nalewajko, K., & Begelman, M. C. 2016, ApJL, 816, L8
Wright, T. P., & Hadley, G. R. 1975, PhRvA, 12, 686
Zenitani, S. 2018, PPCF, 60, 014028
Zenitani, S., & Hesse, M. 2008, PhPl, 15, 022101
Zhang, B., & Yan, H. 2011, ApJ, 726, 90
Zhang, H., Li, X., Guo, F., & Giannios, D. 2018, ApJL, 862, L25

[9] Note that the Hall quadrupole field does not ease the pressure depletion at the x-line, since it vanishes right at the x-line.